Research Article

Environmental Chemistry and Safety
DOI: 10.26599/ECS.2026.9600024
2026, 2, 9600024

Photoelectrochemical Degradation of Glyphosate Using Schottky Heterojunction between MXene and Graphitic Carbon Nitride Based Photocatalyst

Akash Srivastava[1], Aditi[2], Pratyush Jain[3], and Priyanka Gupta[2*]

[1]Department of Chemical Engineering, Indian Institute of Technology Patna, Patna 801106, India
[2]Department of Chemical Engineering, Harcourt Butler Technical University Kanpur, 208002, India
[3]Ottovodia Private Limited, Kanpur, 208011, Uttar Pradesh, India

Abstract: Glyphosate is one of the most commonly used herbicides that is frequently observed in soil and water systems. Its persistence and toxicity pose serious concerns to human health and the environment. Conventional treatment methods such as adsorption and biological processes are often inadequate as these approaches either transfer the pollutant to another phase or show partial mineralization. In this work, MXene ($Ti_3C_2T_x$) and graphitic carbon nitride (g-C_3N_4) supported over activated carbon fibre (ACF) were integrated to create a Schottky-type heterojunction as a stable photoanode for photoelectrochemical (PEC) degradation of glyphosate. For single-chamber PEC operation, g-C_3N_4 served as the visible-light absorber, metallic MXene acted as an electron sink while ACF as a conductive and sustainable support. Strong interfacial coupling between MXene and g-C_3N_4 was established by structural and spectroscopic investigations that supported band bending at the interface and enabled effective charge separation. The hybrid system accelerated the oxidation of glyphosate by significantly increasing the production of reactive oxygen species. Under ideal conditions, glyphosate was degraded to around 100% in 270 min at a bias potential of 1.4 V. These findings highlight the potential of MXene-g-C_3N_4/ACF photoanode as a scalable, cost-effective, and visible light active platform for remediation of glyphosate and potentially other organic contaminants in water.

Key words: Photocatalysis; Schottky barrier; Glyphosate degradation; MXene; Graphitic carbon nitride; Schottky heterojunction

Citation: Srivastava A, Aditi, Jain P, et al. Photoelectrochemical Degradation of Glyphosate Using Schottky Heterojunction between MXene and Graphitic Carbon Nitride Based Photocatalyst. *Environmental Chemistry and Safety*, 2026, 2, 9600024. https://doi.org/10.26599/ECS.2026.9600024

1. Introduction

N-(phosphonomethyl) glycine (PMG) or glyphosate is a widely used broad-spectrum herbicide extensively used in modern agricultural weed management. It inhibits the shikimate pathway, a vital route present in plants, fungi, and some microorganisms [1]. Its widespread use has raised several concerns regarding environmental persistence, toxicity, and challenges in degradation. PMG possesses high water solubility (~11.6 mg/L at 25°C) that facilitates its rapid transport through soil and water systems that intensify contamination risks [2]. The European Union (EU) has set a rigorous threshold of 0.1 µg/L for PMG in drinking water due to its toxicity and widespread detection [3, 4]. However, concentrations exceeding regulatory thresholds have been recorded globally. In some regions PMG levels in groundwater is found to be ~76 mg/L in container effluent from herbicide containers [5]. PMG has been detected in surface freshwater bodies across Europe at concentrations of approximately 50 µg/L [6, 7]. In agricultural pond systems, reported PMG levels range from 12–221 µg/L in Argentina and up to 427 µg/L in the USA, while concentrations near agricultural regions in Brazil reach as high as 2160 µg/L [8-10].

PMG and its primary metabolite aminomethylphosphonic acid (AMPA) are known for its persistence and toxicity [11]. Both compounds can affect non-target organisms, disrupt soil microbial communities and impair ecological functions such as nutrient cycling and soil fertility [9,12, 13]. PMG has also been associated with endocrine disruption, biodiversity loss, and potential carcinogenicity, according to the International Agency for Research on Cancer (IARC) [14, 15]. Various studies have reported that even trace concentrations (<0.02 mg/L) may lead to endocrine disruption and carcinogenic outcomes in humans [16, 17]. These data underscore the urgent need for efficient technologies to remediate PMG-contaminated water before levels become unmanageable.

Addressing the environmental impact of PMG requires effective degradation strategies. In this context, conventional treatment methods such as adsorption, biological treatment, and advanced oxidation processes (AOPs) have been applied for PMG removal and degradation [18-20]. For instance, adsorption-based approaches using materials like biochar, metal organic frameworks (MOFs), and ion-exchange resins offer simplicity and cost-effectiveness [21, 22]. However, these methods are non-destructive and generate secondary waste. For

Correspondence to: Gupta P, priyankamnit936@gmail.com
Received: October 10, 2025; Revised: March 16, 2026; Accepted: March 30, 2026

example, Fe^{3+}-preloaded D151 resin demonstrated high adsorption capacity (481.85 mg/g) in saline water [23]. Despite its high efficiency and salt resistance, the adsorption process proved non-destructive and failed to degrade PMG molecules. This limits its suitability for complete detoxification particularly in comparison to approaches focused on complete degradation of pollutants.

However, AOPs enable effective mineralization of PMG through generation of highly reactive radicals including hydroxyl species (•OHs) that are capable of degrading complex organics to simpler and less harmful molecules [24]. Among AOPs, photocatalysis and electro-oxidation have emerged as the most widely studied methods for PMG degradation in aqueous systems [25-30]. However, traditional photocatalysts like TiO_2 face challenges such as wide bandgap, fast electron-hole recombination, and reduced performance under visible light [31, 32]. Therefore, recent advancements have been introduced focussing on designing hetero-structured systems to overcome the intrinsic limitations of single-component photocatalysts [33, 34]. These limitations include wide band gaps, high rates of photogenerated charge recombination, and reduced catalytic activity under visible light [35]. Development of a heterojunction has emerged as a powerful tool to improve photocatalytic efficiency by promoting charge separation. Early developments led to type-II heterojunctions where photogenerated holes and electrons transfer between semiconductors based on its band positions [36, 37]. However, this design had several flaws such as thermodynamic instability and deviation between theoretical and actual charge transfer pathways [38]. The *Z-scheme* mechanism, though an improvement, still shows low efficiency due to the use of electron mediators [39].

In contrast, metal-semiconductor systems based on Schottky junction provide a simpler and effective alternative. These junctions form when a semiconductor comes in contact with a metal possessing a lower work function that results in the development of a Schottky barrier [40]. This barrier drives unidirectional transfer of electrons to the metal from the semiconductor that promotes charge separation and suppress recombination [41]. Such interfaces are particularly effective in photocatalysis where the metal acts as an electron sink enabling the accumulation of electrons that participate in redox reactions with targeted pollutants. For instance, a Schottky junction was constructed between Sn–Bi–MOF and MXene in a recent study enabled directional electron transfer and enhanced charge separation [42]. The system achieved 96.2% tetracycline degradation in 90 min under visible light demonstrating the effectiveness of Schottky-based structure for photocatalytic pollutant removal.

In this study, a composite photocatalyst comprising MXene ($Ti_3C_2T_x$) and graphitic carbon nitride (g-C_3N_4) supported over activated carbon fibre (ACF) was engineered to construct a Schottky junction for enhanced photoelectrochemical (PEC) degradation process. This novel catalyst was applied for the first time for the PEC degradation of PMG, a widely used and environmentally persistent herbicide. The MXene–g-C_3N_4 composite has emerged as promising photocatalyst owing to its synergistic structural and electronic characteristics [43]. Incorporation of g-C_3N_4 with MXene facilitates improved visible-light absorption and enhances the migration and separation of photogenerated charge carriers [44, 45]. The MXene–g-C_3N_4 interface forms a Schottky junction due to the fermi level difference between the two materials. This junction facilitates unidirectional electron transfer from the conduction band of g-C_3N_4 to the metallic MXene surface. [46]. The formation of this junction promotes spatial charge separation and suppresses recombination losses, thereby enhancing photocatalytic efficiency across diverse environmental systems. Notably, g-C_3N_4 has gained significant attention due to its role as a visible-light-active photocatalyst [47]. It offers a suitable bandgap and visible-light activity therefore, serves as an efficient semiconducting photo absorber [48, 49]. Nevertheless, bulk g-C_3N_4 often shows limited photocatalytic performance [47]. The main reason is the inefficient separation and slow transfer of photogenerated charge carriers. These limitations reduce its overall activity under light irradiation. To overcome this limitation, g-C_3N_4 is widely incorporated to heterojunction systems. Such configurations enhance interfacial charge transfer and reduce recombination losses. On the other hand, MXene functions as the electron sink owing to its metallic conductivity and favourable electronic structure [47, 50]. MXene possesses the potential to couple with semiconductor photocatalysts and results the formation of a Schottky junction [51]. Formation of such junction significantly promotes efficient separation of photoinduced charge carriers, thereby improve photocatalytic performance of the catalyst. In the present study, by integrating MXene with g-C_3N_4 to form a Schottky-type photocatalyst, this work aims to demonstrate enhanced PEC degradation of PMG, improved redox efficiency, and reduced electron–hole recombination. This approach contributes to the development of economical and scalable catalysts for advanced wastewater treatment technologies.

2. Materials and methods

Urea (NH_2CONH_2), di-sodium tetraborate decahydrate ($Na_2B_4O_7.10H_2O$), sodium chloride (NaCl), potassium chloride (KCl), lithium fluoride (LiF), hydrochloric acid (HCl) and di-sodium hydrogen phosphate (Na_2HPO_4) were procured from Merck, India. 9-fluroenylmethyl chloroformate (97%) (FMOC-Cl) was purchased from Sigma Aldrich, India. Phenolic precursor-derived activated carbon fibres (ACF) were supplied by Nippon Kynol Inc. (Japan). Ti_3AlC_2 MAX phase powder was purchased from Nanochemazone Inc, Canada. Sodium sulfate (Na_2SO_4), and acetonitrile (ACN, HPLC grade) were obtained from SRL Pvt. Ltd., India. Nafion 117 was procured from Sinsil International, India. The ultrapure Milli-Q water was obtained from the purification system installed at the Indian Institute of Technology, Patna India.

2.1. Catalyst preparation

The first component, g-C_3N_4 was prepared via thermal polymerization of urea. [52, 53]. Briefly, an initial mass of 10 g urea was carefully wrapped in an aluminium foil. The wrapped sample was then placed inside a tubular reactor furnace. The heating was carried out at a ramp rate of 4.6°C per min until 550°C was attained. Upon reaching the target temperature, the sample was held at 550°C for 3 h to ensure complete polymerization. Following heat treatment, the sample underwent natural cooling until ambient conditions were attained.

The procedure described in a published study was

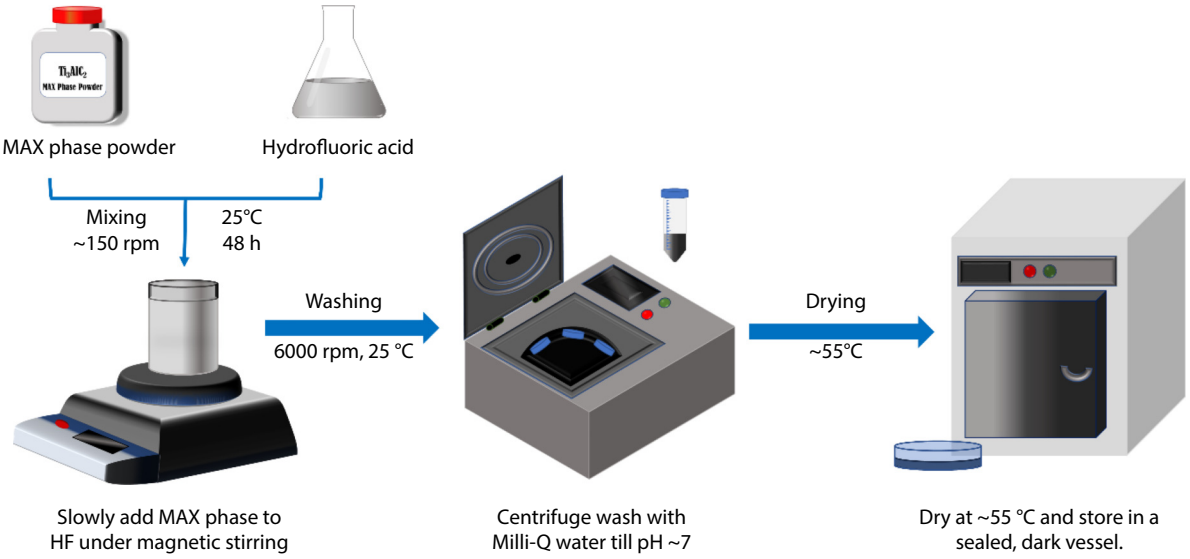

Fig. 1. Preparation of MXene using chemical etching process. HF produced from LiF and HCl.

employed to etch the aluminum layers and delaminate the MXene with slight modifications as illustrated in Figure 1 [54]. MXene was prepared using chemical etching of Ti_3AlC_2 with *in-situ* hydrofluoric acid produced from LiF and HCl. Initially, 2 g of Ti_3AlC_2 was measured accurately. This powder was slowly added to a mixture of LiF and HCl. The addition was done gradually to ensure controlled exothermic reaction and safety. The mixture underwent constant agitation at 150 rpm. The reaction was carried out at room temperature and maintained for 48 hours. After completion of the etching process, the resultant dispersion was subjected to repeated washing. Milli-Q water was used for washing, and centrifugation was performed at 6000 rpm during each cycle. Washing was carried out repeatedly until the supernatant exhibited a neutral pH. The resulting solid residue was then separated and dried overnight to yield MXene.

The photocatalyst was synthesized by combining MXene and g-C_3N_4 in equal proportions (Figure 2). For this purpose, 0.5 g each of MXene and g-C_3N_4 were precisely measured with a digital analytical balance. Each material was then subsequently placed in individual centrifuge tubes. The process was followed by the addition of 50 mL of deionized (DI) water to each tube to prepare uniform suspensions. The tubes were securely capped to avoid contamination. The two suspensions were poured to a clean reaction flask. The combined mixture was then stirred using a magnetic stirrer. The stirring speed was maintained at 400 rpm. Continuous stirring was carried out for 24 hours. This prolonged stirring allowed proper mixing as a result uniform dispersion of MXene within g-C_3N_4 [55]. The resulting material was considered as the final MXene–g-C_3N_4 photocatalyst.

The photoanode was prepared by coating the synthe-

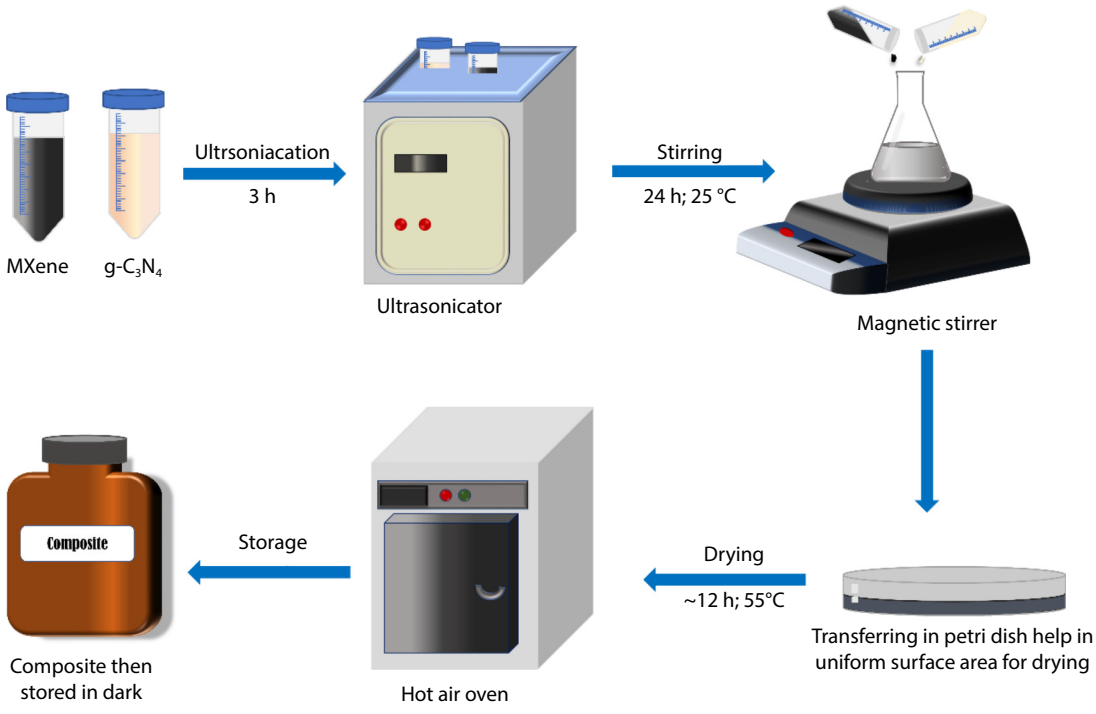

Fig. 2. Schematic diagram illustrating the preparation process of MXene–g-C_3N_4.

sized photocatalyst on ACF. The ACF cloth used as the substrate measured 1.5 × 3.5 cm^2. The catalyst ink for coating was prepared by dispersing the photocatalyst in 50 mL of isopropanol (IPA) at a concentration of 1 mg/mL. Subsequently, 50 µL of Nafion binder was added to promote adhesion of the photocatalyst on the ACF surface. The mixture was then subjected to constant stirring for 3 hours to ensure homogeneous dispersion of the photocatalyst within the solution. The resultant catalyst ink was carefully drop-casted on ACF surface ensuring uniform distribution of the photocatalyst over the substrate. The coated electrode was dried at 50°C. The drying process ensured proper adhesion and formation of a stable catalyst layer on ACF surface.

2.2. Material characterization

The physicochemical characteristics of the prepared materials were thoroughly investigated using several characterization techniques. The field emission scanning electron microscopy (FESEM, JEOL model JSM-7800 F) was employed to analyze surface morphology and microstructural features at high resolution. Crystallinity and lattice orientation were examined via selected area electron diffraction (SAED) pattern, facilitating insight to the ordered regions within the nanostructures. High-resolution transmission electron microscopy (HRTEM, FEI Tecnai G2) provided nanoscale imaging of the lattice structure, enabling visualization of interplanar spacing. Bright-field and dark-field modes were utilized to enhance contrast and delineate structural heterogeneities. X-ray photoelectron spectroscopy (XPS, K-th PHI 5000 Versa Prob II, FEI inc., USA) was conducted to analyze the surface elemental composition and oxidation states. The binding energy scale was referenced to the C1s peak at 284.6 eV, corresponding to sp^2 hybridized carbon. Fourier transform infrared spectroscopy (FTIR, Perkin Elmer Spectrum Two) was performed in transmittance mode to identify functional groups and evaluate chemical bonding interactions. The crystalline phase and structural composition were analyzed using X-ray diffraction (XRD, X'Pert Pro, PANalytical). The obtained diffraction patterns were matched against standard reference data to confirm phase identity and evaluate crystallinity.

Optical absorption properties and bandgap energies of the material was evaluated by constructing a Tauc plot, where the Kubelka–Munk function was plotted against photon energy ($h\nu$), and the relationship was analyzed using the following expression: $\alpha h\nu = k(h\nu - E_g)^{n/2}$ where, E_g denotes the estimated bandgap energy, k represents a non-zero constant related to the absorption edge, ν is the frequency of incident light, h is Planck's constant, and α stands for the absorption coefficient [52]. All electrochemical analysis was performed using potentiostat (Autolab 302 N, Metrohm India Ltd, Netherlands). Electrochemical behaviour of the synthesized materials was preliminarily assessed using CV. The CV measurements were carried out using a conventional three-electrode configuration. A glassy carbon electrode coated with the test materials was used as the working electrode. An Ag/AgCl electrode and a platinum rod were employed as the reference and the counter electrodes respectively. Phosphate buffer solution was used as the electrolyte. The CV curves of MXene, g-C_3N_4, and MXene–g-C_3N_4 samples were recorded in the potential range of −2 to +2 V. Mott Schottky plots were obtained in 0.5 M Na_2SO_4 solution at a frequency of 1000 Hz. Photoelectrochemical tests were taken in 1 M Na_2SO_4 solution, and the cell was illuminated with a solar simulator (ORIEL, Sol 3 A, Newport suppliers, Netherlands). For the determination of organic matter present in the samples, Chemical Oxygen Demand (COD) removal analysis was performed using the standard potassium dichromate method. Assessment of PMG mineralization were done using Total Organic Carbon (TOC) analyzer (Shimadzu, Japan 5050). Prior to TOC analysis, samples were filtered using 0.22 µm filter. To analyse the final mineralization products ion identification was done using ion chromatograph (Metrohm Eco IC 925).

2.3. Experimental setup

PMG degradation was performed in a batch-type single-chamber PEC reactor. The system was configured with a three-electrode setup. The prepared working electrode was fixed using a Teflon frame and connected through a brass rod. A platinum rod served as the counter electrode while an Ag/AgCl electrode was employed as the reference electrode. The reactor was filled with 200 mL of an aqueous solution containing 50 mg/L PMG and 0.05 M sodium sulfate as the supporting electrolyte. A 25 W LED lamp as the light source was used for photocatalysis. During the experiment, a constant magnetic stirrer was used to ensure uniform mixing of the reaction solution. The configuration of the electrical connections in the PEC reactor was adapted from a previously reported setup [56]. The reference electrode (Ag/AgCl) was inserted in the solution and positioned close to the working electrode. The applied bias potential was controlled using an external DC power supply. A digital multimeter was used for independent monitoring of the potential difference between the working and reference electrodes. The setup allowed precise control and real-time measurement of the PEC parameters during the reaction.

The reaction was performed for 2 hours under continuous illumination and stirring. Aliquots of 2 mL were withdrawn every 30 min to monitor PMG degradation. Each sample underwent a derivatization step using FMOC-Cl [16]. Derivatization was performed by mixing 2 mL of the sample with 2 mL of FMOC-Cl solution followed by the addition of 1.25 mL borate buffer. The mixture was vortex for 5 min to ensure proper derivatization followed by washing with diethyl ether. The upper layer was discarded and the washing step was repeated. Subsequently, 1 mL of the bottom aqueous layer was collected and mixed with 3 mL of borate buffer. The final mixture was analyzed using UV–visible spectroscopy at 264 nm to observe the degradation progress.

3. Results and discussion

The surface morphology of the prepared materials was investigated using FESEM as shown in Figure 3. The bare ACF exhibits a smooth, cylindrical surface with no visible surface irregularities, indicating its pristine nature (Figure 3a). This surface served as a suitable support for active material deposition. The synthesized g-C_3N_4 resulted in formation of agglomerated, wrinkled nanosheets with a high degree of surface roughness (Figure 3b). These features suggest a high surface area that supports improved interaction with co-catalysts or charge carriers. The SEM image of MXene displays a characteristic layered, partially delaminated morphology with well-defined inter-

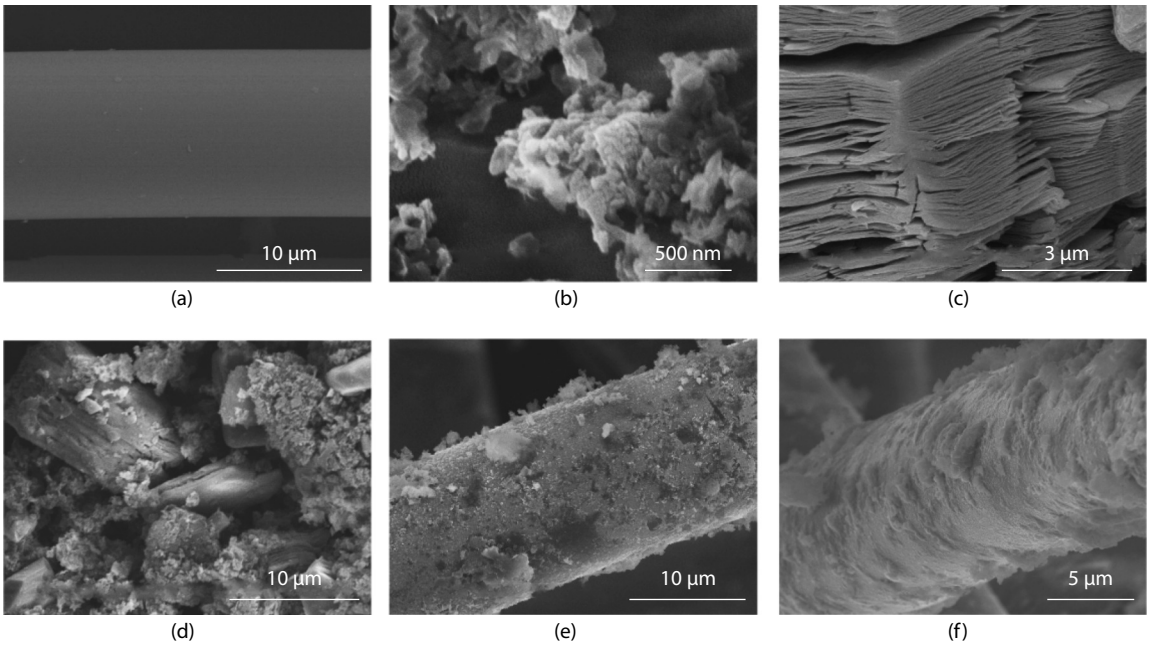

Fig. 3. FESEM images of: (a) Bare ACF showing smooth fibrous texture; (b) g-C_3N_4 with aggregated, wrinkled nanosheets; (c) MXene exhibiting layered, exfoliated morphology; (d) MXene-g-C_3N_4 showing rough, heterogeneous surface; (e) MXene–g-C_3N_4 coated on ACF, forming an adherent layer; and (f) high-magnification image of (e) revealing a dense, nanostructured coating.

layer spacing, indicating successful etching and exfoliation (Figure 3c). Such morphology improves electrical conductivity and offers abundant active sites. The SEM image of MXene–g-C_3N_4 presents a heterogeneous and rough surface (Figure 3d). The g-C_3N_4 particles were visibly embedded within or deposited on MXene layers indicating the interfacial contact between g-C_3N_4 and MXene. It combines the ability of g-C_3N_4 to drive photocatalysis under visible light with the electrical conductivity and redox-active surfaces of MXene. This hybrid morphology is anticipated to enhance charge separation and facilitates photogenerated electron transport. Figure 3e shows that drop-casting of MXene–g-C_3N_4 solution on ACF produced a relatively uniform coating on the fibrous carbon surface. At higher magnification (~5.0 µm) the MXene–g-C_3N_4 film appeared densely packed with nanoscale roughness (Figure 3f) confirming strong adhesion and coverage over the ACF. surface.

TEM analysis was used to investigate the topographical characteristics of the MXene–g-C_3N_4 sample providing detailed insights in its layered structure and interfacial contact between the components. The dark-field image shows well-dispersed MXene–g-C_3N_4 particles with bright contrast as seen in Figure 4b, indicating the presence of crystalline domains within the MXene–g-C_3N_4 sample. These bright zones suggest the presence of nanocrystalline features dispersed across the matrix. The corresponding bright-field image revealed a layered and aggregated structure, typical of 2D materials (Figure 4a). The HRTEM image of the MXene–g-C_3N_4 sample displays clear lattice fringes with well-defined interlayer spacing thereby confirming the successful integration of both materials at the nanoscale (Figure 4c). The SAED patterns further provide insights to the crystallinity of the MXene–g-C_3N_4 sample. The SAED pattern in Figure 4d shows discrete diffraction spots and ring-like patterns, indicating polycrystalline regions of MXene within the MXene–g-C_3N_4 sample. The presence of both diffuse and sharp diffraction features suggested a mixed-phase structure with amorphous g-C_3N_4 regions and crystalline MXene domains coexisting.

CV was performed to examine the electrochemical behaviour and charge transfer characteristics of MXene, g-C_3N_4, and the MXene–g-C_3N_4 heterostructure (Figure 5a). The hybrid electrode exhibited a higher current response than the individual components that reflected the improved electrochemical activity and faster interfacial charge transfer. MXene acts as an electron sink due to its high electrical conductivity, thereby facilitating directional electron transfer from g-C_3N_4 and improving the overall charge separation efficiency of the heterostructure. The enhanced current density at anodic potentials >1.2 V versus Ag/AgCl is consistent with the optimum bias (1.4 V) required for maximum PEC degradation of PMG. It confirmed the role of MXene in facilitating directional electron transport and suppressing recombination. The quasi-rectangular CV profile without sharp redox peaks indicates capacitive-dominated behavior with overlapping Faradaic contributions suggesting stable operation and efficient charge storage/transfer processes. These results validated that the Schottky junction between MXene and g-C_3N_4 promotes favorable charge dynamics for driving reactive oxygen species (ROSs) generation during PEC degradation.

The optical band gaps of MXene, g-C_3N_4, and the MXene–g-C_3N_4/ACF were determined using Tauc plots constructed from UV–Vis absorption spectra (Figure 5b). The g-C_3N_4 sample exhibited a direct band gap of ~2.96 eV. The observed band gap corresponds closely to values documented in prior studies on g-C_3N_4 photocatalysts [57, 58]. MXene showed a significantly lower band gap near 0.87 eV, confirming its metallic or narrow-gap semiconducting nature. The MXene–g-C_3N_4 sample presented a slightly reduced band gap of 2.89 eV compared to pristine g-C_3N_4. This decrease in band gap value suggests improved absorption of visible light and enhanced interfacial charge transfer. The shift in the absorption edge of the MXene–g-C_3N_4 indicates electronic interaction among the components. Such narrowing of the band gap

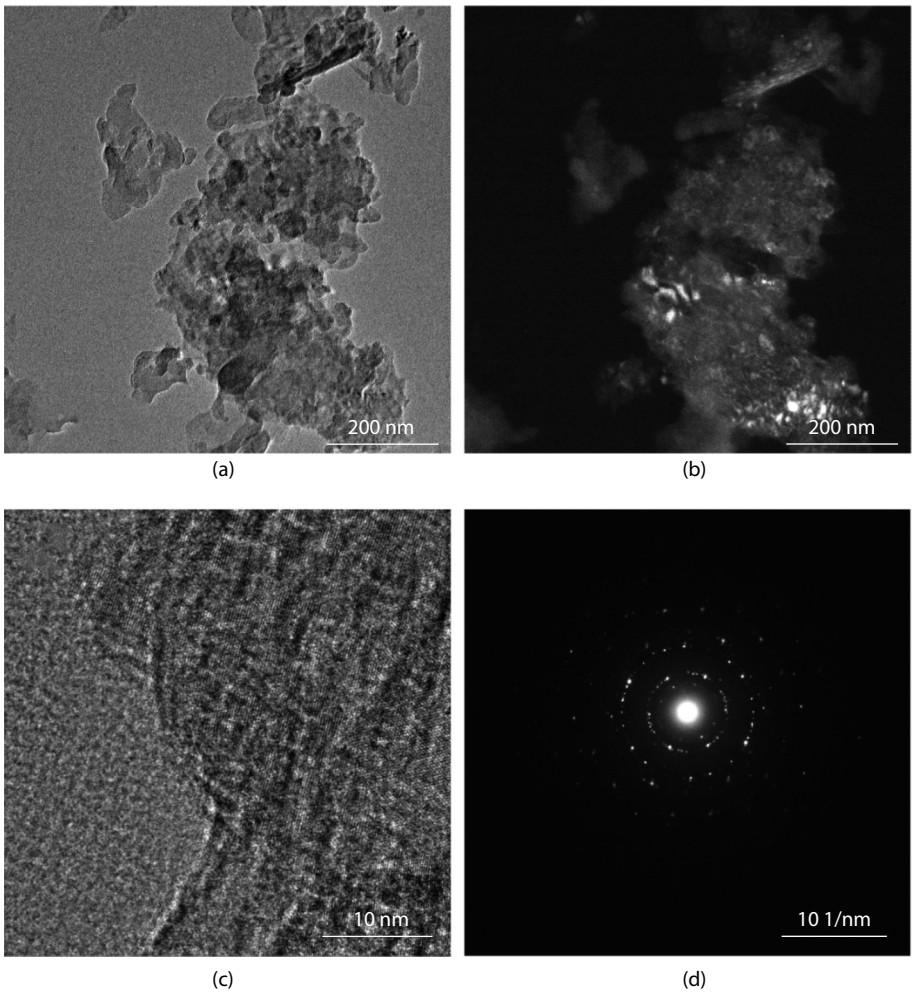

Fig. 4. TEM images of the g-C_3N_4–MXene sample: (a) Bright-field image illustrating layered morphology; (b) dark-field image showing crystalline domains; (c) HRTEM image with visible lattice fringes; and (d) SAED patterns showing polycrystalline features.

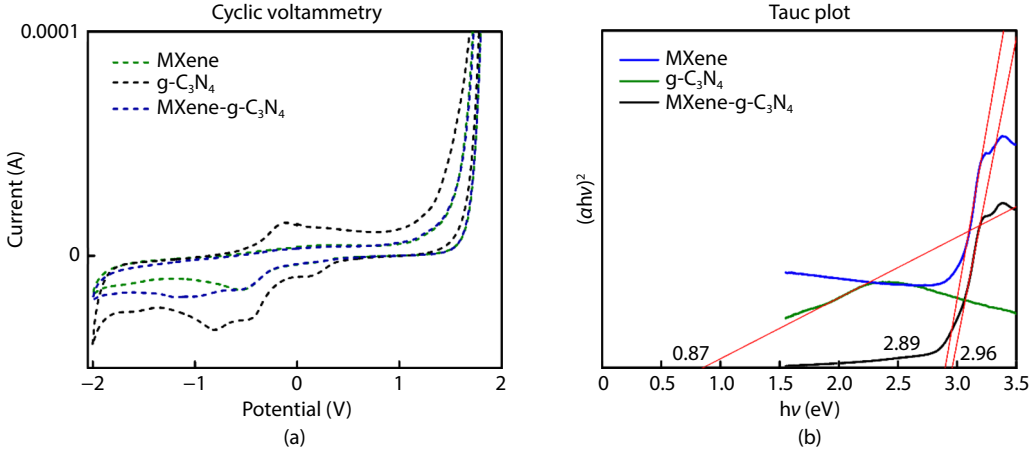

Fig. 5. (a) CV curves of g-C_3N_4, MXene, and MXene–g-C_3N_4 electrodes in 0.1 M phosphate buffer measured using a three-electrode setup; and (b) Tauc plots of g-C_3N_4, MXene, and MXene–g-C_3N_4/ACF showing optical absorption characteristics and edge shifts.

proves favorable for photocatalytic applications under solar irradiation.

To quantitatively evaluate the enhancement in the active sites following MXene incorporation onto electrode, a capacitive study of the catalyst was further performed. CV measurements for g-C_3N_4 and MXene–g-C_3N_4 coated over ACF were conducted at different scan rates ranging from 0.005 to 0.10 V/s (Figure S5a, b) to evaluate their double-layer capacitance. The capacitive current was extracted from the non-Faradaic potential region for both the materials. The current showed a linear dependence on the scan rate according to the relationship $i=C_{dl}v$, where i represents the capacitive current, C_{dl} is the double-layer capacitance, and v is the scan rate. The slope obtained, i.e., C_{dl}, from the linear fitting corresponding to MXene–g-C_3N_4 and g-C_3N_4 was found to be 58.44 μF and 46.42 μF, respectively (Figure S5c). Furthermore, electrochemi-

cal active surface area (ECSA) can be calculated as ECSA = C_{dl}/C_s, where C_s is the specific capacitance of standard electrode materials on a unit surface area. C_s can be considered equal for both the catalysts based on reported literature [59]. This implies that ECSA of MXene–g-C_3N_4 is 1.25 times larger than that of g-C_3N_4. Significantly improved ECSA of MXene–g-C_3N_4 heterostructure indicates the provision of more abundant electrochemically accessible sites. Enhanced ESCA coupled with the high electrical conductivity of the MXene acting as an electron sink, facilitated the rapid interfacial electron transfer and reduced charge recombination.

To get a better mechanistic insight of the charge transfer within the engineered heterojunction relative band structure alignment is studied. The conduction and valence band positions are calculated using Butler and Ginley relationship [60].

$$E_{VB}=X-E^{e}+0.5E_g \quad (a)$$

$$E_{CB}=E_{VB}-E_g \quad (b)$$

E_{VB} is valence band (VB) edge potentials; E_{CB} is conduction band (CB) edge potentials; E_g is the band gap energy of semiconductor; X is the Mulliken electronegativity of semiconductor and E^e represents energy of free electrons on hydrogen scale (4.5 eV). The Mulliken electronegativity of g-C_3N_4 is 4.72 eV, as obtained from the literature [61]. Eg, calculated from the tauc plots, is 2.96 eV. The corresponding E_{CB} and E_{VB} values thus obtained are -1.26 V and 1.7 V, respectively. The work function of MXene with F terminations is reported to be around +0.15 eV vs NHE [62]. Further, Mott-Schottky plots were obtained to calculate the flat band potential (E_{fb}) of g-C_3N_4 coated over ACF. It reveals the affinity of electron migration from g-C_3N_4 towards MXene. In Figure S6a, the positive slope of Mott Schottky plot demonstrates g-C_3N_4 to be a n-type semiconductor. From the x-intercept E_{fb} of g-C_3N_4 was calculated to be −1.22 V vs Ag/AgCl.

$$E_{NHE}=E_{Ag/AgCl}+0.197 \quad (c)$$

From eq. c, E_{fb} of g-C_3N_4 was calculated to be −1.023 V vs NHE [63]. Because of high density of electrons in n-type semiconductors E_{fb} is generally found close to E_{CB} edge [64].

The favourable energy band alignment shows the optimal conditions for electron migration from CB of g-C_3N_4 to the Fermi level of MXene. On the formation of heterojunction Fermi level of both g-C_3N_4 and MXene will align and result in upward bending of the CB and VB of g-C_3N_4. This creates an internal electric field and a Schottky barrier, which facilitates the efficient separation of photogenerated carriers by trapping electrons in the metallic MXene and suppressing charge recombination [47].

Chopped light photocurrent measurements were made for g-C_3N_4 and MXene–g-C_3N_4, both coated over ACF. Catalysts deposited over ACF were illuminated under solar radiation in a regular interval of 60 seconds. As shown in Figure S6b, the current response increased with the solar light on, achieving a stable plateau region and decays slowly in the dark. The photocurrent density of MXene–g-C_3N_4 can be observed to be three times higher than that of pristine g-C_3N_4. This rapid and stable response provides direct evidence of a stable heterojunction formation and enhanced charge migration from g-C_3N_4 towards MXene.

The FTIR spectra of MXene, g-C_3N_4, MXene–g-C_3N_4 composite, and ACF are presented in Figure 6a. A broad band in the region of 3000–3500 cm^{-1} was observed at the spectra of g-C_3N_4 and the MXene–g-C_3N_4 samples attributed to the N–H stretching of terminal –NH_2 groups, commonly found in g-C_3N_4 structures [65]. The peaks in the range of 1632–1400 cm^{-1} were related to C–N and C=N stretching modes indicating the presence of aromatic nitrogen heterocycles [66, 67]. The band observed from 1230 to 1402 cm^{-1} indicates C–N(–C) or C–NH–C stretch [66, 67]. The other bands observed at 1200 and 800 cm^{-1} in g-C_3N_4 and MXene–g-C_3N_4 samples may contain triazine section [68, 69]. The band appeared at 1450 cm^{-1} in the spectrum of ACF indicates CH bending vibrations. The signal at 1060 cm^{-1} corresponded to C–OH and C–O–C stretching indicating oxygen-containing surface functionalities on ACF [70]. The FTIR spectrum of MXene shows a peak ~597 cm^{-1} corresponded to Ti–O bond deformation i.e., a typical feature of Ti-based MXene materials [71]. The MXene–g-C_3N_4 spectrum combined the features of g-C_3N_4, MXene, and ACF. It showed peaks from all components without significant shifts and referring the successful incorporation of MXene–g-C_3N_4 within the ACF.

The XRD pattern of g-C_3N_4 displayed characteristic peaks at 13.09° and 27.83°, corresponding to the (100) and (002)

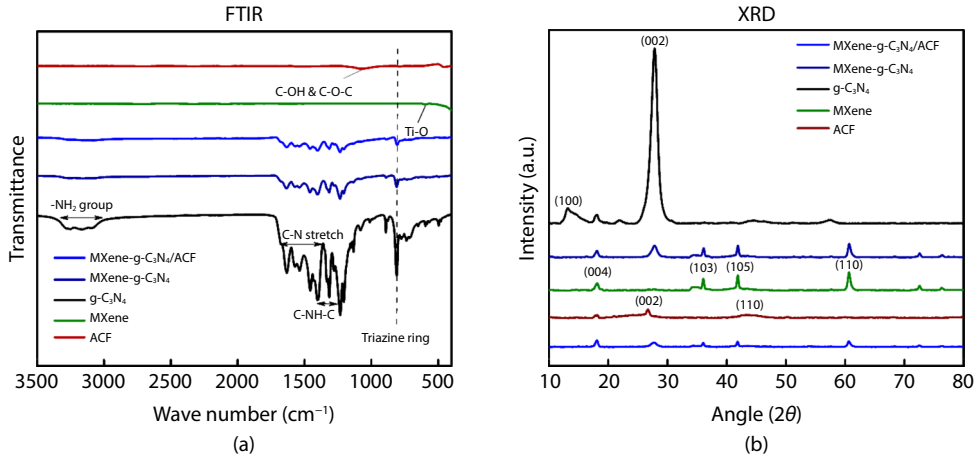

Fig. 6. (a) FTIR analysis of prepared materials; (b) XRD pattern of g-C_3N_4, MXene, MXene–g-C_3N_4 and MXene–g-C_3N_4/ACF.

planes respectively (Figure 6b). The (100) reflection is ascribed to in-plane structural arrangement of tri-s-triazine units. Another prominent peak (002) signifies the interlayer accumulation of conjugated aromatic domains along the graphitic direction consistent with a layered structure of g-C_3N_4 [72, 73]. The XRD profile of MXene shows a dominant peak at 18.1° attributed to the (004) plane, confirmed successful etching of the Al layer from the MAX phase [74]. The other peaks at 36.15° (103) and 41.8° (105) indicates residual TiC phases derived from the parent Ti_3AlC_2 structure, as reported in a recent study [75]. The XRD pattern of ACF displayed two distinct peaks at 2θ ≈ 26.7° and 43.5°, assigned to the (002) and (110) lattice planes, respectively. These peaks signify the graphitic nature of the carbon framework, indicating the presence of well-ordered graphitic domains within the ACF matrix. The fabricated hybrid structure of MXene–g-C_3N_4 sample shows peak at 2θ ≈ 27.83° from g-C_3N_4 and another peak at 2θ ≈ 18.1° from MXene suggesting the successful integration of both phases without structural disruption. The crystallite dimension of the synthesized MXene–g-C_3N_4 sample was estimated from the XRD pattern using the Scherrer equation, $D = K\lambda/\beta\cos\theta$; where D is the crystallite dimension, K is the Scherrer constant, λ is the X-ray wavelength, θ is the Bragg angle and β is the full width at half maximum (FWHM) of the diffraction peak (in radians) [76]. Based on the XRD data, the average crystallite dimension was found to be 15.65 nm. In the MXene–g-C_3N_4/ACF electrode, the diffraction pattern combined the characteristic peaks of all three components, with noticeable retention of the (002) peak from g-C_3N_4, the (004) and TiC-associated peaks from MXene, and the (002), (110) features from ACF. These data confirmed the successful fabrication of a hybrid heterostructure incorporating g-C_3N_4, MXene, and ACF.

The XPS profiles of C1s, Ti2p, F1s, O1s, and N1s in g-C_3N_4, MXene, ACF, MXene–g-C_3N_4/ACF, and the MXene–g-C_3N_4 composite were investigated through deconvolution of its cumulative peaks. The detailed deconvolution results for MXene–g-C_3N_4 are presented in the main manuscript (Figure 7), while those for the other materials are provided in the supplementary file (Figures S1–S4). The C1s spectrum for g-C_3N_4 contains five peaks located at 284.9, 286.3, 288.3, 289.1 and 293.6 eV, correspond to the adventitious graphitic carbon (C–C), C–NH_2, N–CN, COOH and localized π–π transition, respectively (Figure S1a) [72, 77, 78]. The MXene exhibited binding energies of 281.8, 284.8, and 286.3 eV, corresponding to Ti–C–Ti, C–C, and C–O bonds, respectively. (Figure S2b) [79]. ACF exhibited C–C, C–O, and C=O functionalities at 284.5, 285.5, and 287.3 eV, respectively (Figure S3a). In the MXene–g-C_3N_4, the energy shift for C1s spectrum can be seen at 284.9, 281.6, 286.4, 288.3, and 289.1 eV that may be the stretches of C–C, C–Ti, C–O, N–CN and C=N respectively (Figure 7c) [79, 80]. The C1s peaks for MXene–g-C_3N_4/ACF showed three components located at 284.7, 288.1, and 288.58 eV assigned to the adventitious graphitic carbon, C=O and N–CN respectively (Figure S4c). In Ti2p region of bare MXene, the binding energies of 455, 455.79, 456.2, 461.1, and 461.4 eV correspond to Ti–C, C–Ti^{2+}–(O/OH), Ti–O, Ti–C ($2p_{1/2}$), C–Ti^{2+}–(O/OH)($2p_{1/2}$), respectively (Figure S2a) [79, 81]. In the XPS specturm of MXene–g-

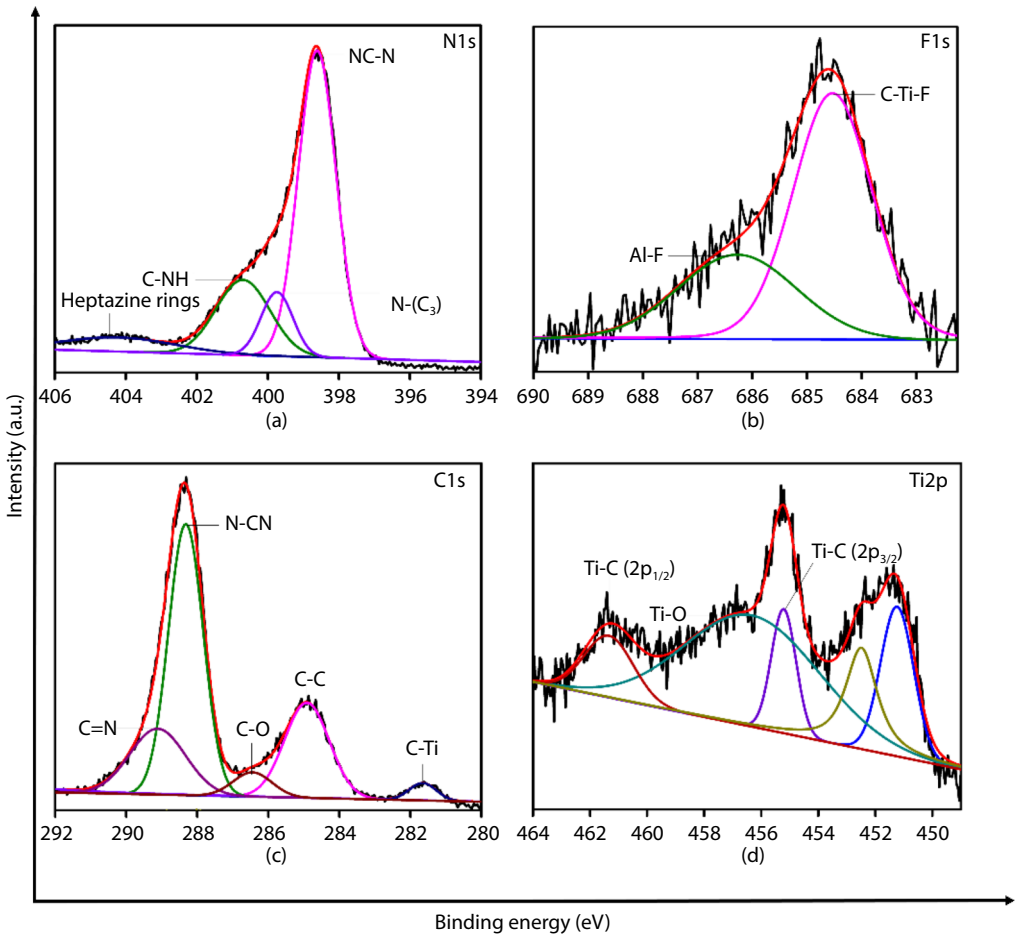

Fig. 7. XPS spectra of N1s, F1s, C1s, and Ti2p in MXene–g-C_3N_4.

C_3N_4/ACF, the binding energies of 455.1, 460.65, and 457.2 eV corresponded to Ti–C, Ti–F_x and C–Ti^{3+} respectively (Figure S4d). The XPS band of the MXene–g-C_3N_4 sample showed signals for Ti2p at 455.2, 456.3 and 461.3 eV indicated to Ti–C ($2p_{3/2}$), Ti–O and Ti–C ($2p_{1/2}$) bonds respectively (Figure 7d). The F1s spectrum of MXene was deconvoluted in two peaks at 685 and 686.4 eV assigned to the C–Ti–F and Al–F bonds respectively (Figure S2c) [79]. These features are typical of fluorine-functionalized MXene following HF etching of the MAX phase [82]. In MXene–g-C_3N_4 sample, the F1s peaks slightly shifted to 684.5 and 686.27 eV (Figure 7b). The downward shift in the C–Ti–F signal suggests modification of the Ti surface environment due to interfacial interaction with g-C_3N_4. After incorporation on ACF, the F1s profile showed peak at 685.35 assigned to the C–Ti–F. The O1s spectrum peaks of ACF were deconvoluted in three peaks at 532.1, 533.5, and 535.9 eV assigned to C=O, O=C–O and C–OH, respectively [83].

3.1. Evaluation of degradation performance

Various comparative experiments were performed under different operational conditions to elucidate the effects of pH variation, light irradiation and electrochemical bias on PMG degradation. TOC and COD removal was also analysed to quantify the degree of PMG mineralization. The mineralization products were further analysed by IC. The influence of solution pH on PMG degradation was investigated in the range of 3 – 11 under PEC conditions (Figure 8a). A pronounced pH dependence was observed with acidic conditions favoring faster degradation. At pH 3, the pollutant concentration decreased sharply and reaching nearly complete removal after 270 min. Degradation efficiency decreased progressively at higher pH values with residual concentrations of ~30% at pH 7, ~50% at pH 9, and >70% at pH 11 post same reaction time. Notably, the enhanced activity under acidic conditions can be attributed primarily to proton-assisted ROS generation with surface charge effects potentially contributing to interfacial interactions. The availability of protons at lower pH facilitates superoxide transformation pathways and promotes efficient interfacial redox reactions leading to improved degradation performance [84]. The point of zero charge (PZC) of the MXene–g-C_3N_4 was determined using the pH drift method and was found to be approximately 3.2 (Figure S7). At pH values below 3.2, the catalyst surface acquires a positive charge. PMG exhibits three dissociation constants (pKa ≈ 2.3, 5.6, and 10.6) and at pH 3 it predominantly exists in its monoanionic form. Acidic medium favoured the electrostatic attraction between PMG and catalyst surface. This promotes the extent of PMG degradation at lower pH level of medium. Moreover, proton-assisted radical transformation pathways promoted at low pH also resulted in augmented interfacial redox reactions contributing to superior degradation efficiency [85]. In contrast, alkaline conditions suppress radical generation and reduce adsorption affinity leading to slower degradation kinetics [28].

The degradation performance of PMG was first evaluated using bare ACF to establish a baseline for comparison. Bare ACF exhibited minimal degradation activity, both under dark and illuminated conditions (Figure 8b). ACF is used as the scaffold because it provides durable yet flexible support with excellent electron mobility and enhanced surface area, ensuring the catalyst is effectively exposed to the reaction medium. To

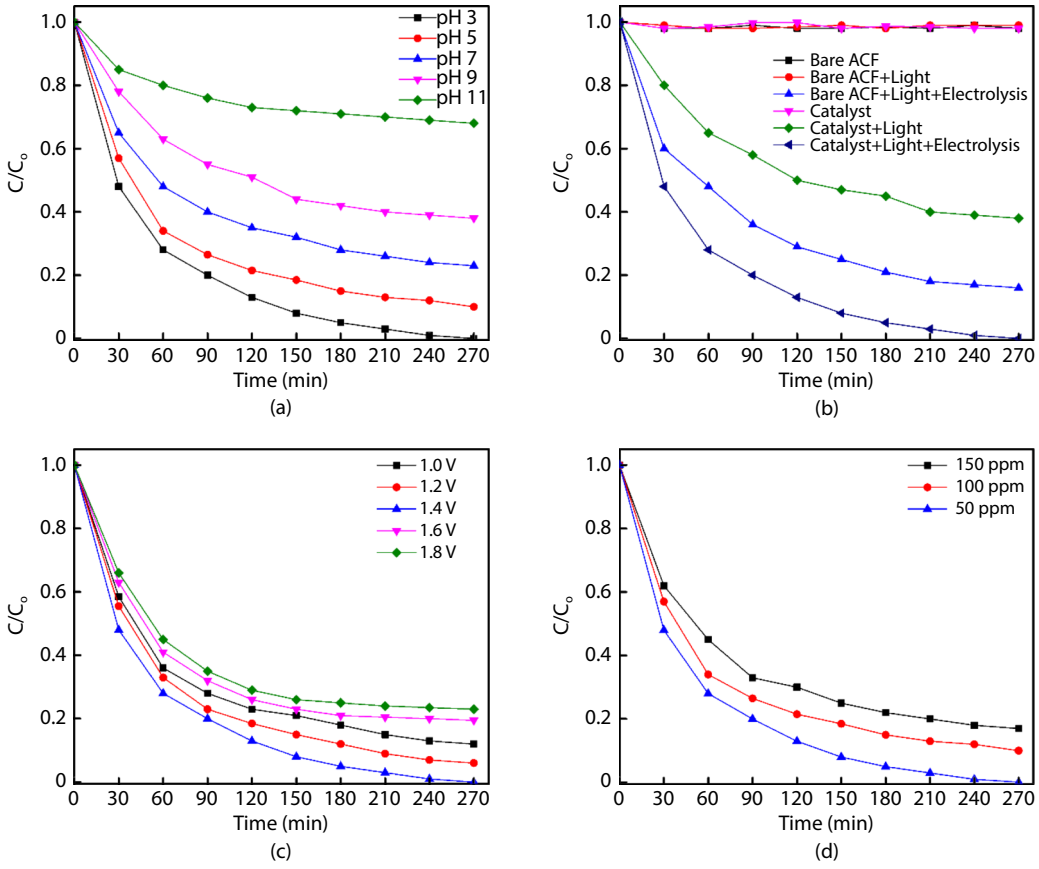

Fig. 8. (a) Effect of pH; (b) Influence of operating conditions; (c) Influence of applied bias potential; (d) Effect of initial PMG concentration on degradation under PEC conditions.

eliminate effect of adsorption, all the degradation experiments were conducted after saturating ACF, catalyst and MXene–g-C_3N_4 coated over ACF with PMG in the dark for 60 mins. This ensured achievement of an adsorption-desorption equilibrium with the working concentration prior to PEC degradation. As shown in Figure 8d, PMG concentration stays nearly unchanged over ACF and catalyst under dark. This confirms that equilibrium is well established. A moderate improvement (~55% degradation) was observed when ACF was used under light irradiation and applied potential suggesting a minor contribution from electrochemical oxidation in the absence of a photocatalyst. This confirmed that neither photolysis nor the individual components possessed sufficient activity for PMG oxidation. Although the addition of the MXene–g-C_3N_4 catalyst and subsequent visible-light exposure resulted in a significant enhancement of degradation efficiency (~65%), confirming its photocatalytic activity. The most significant degradation was achieved under PEC conditions where simultaneous application of light and external bias in the presence of the catalyst resulted in ~100% PMG removal within 270 min. This enhancement can be attributed to more effective separation of photoexcited charge carriers promoting the generation of ROSs and accelerating oxidation of PMG.

The effect of applied bias potential was evaluated in the range of 1.0 – 1.8 V (Figure 8c). The external bias enhanced the band bending within the semiconductor depletion region at the metal–semiconductor junction [86]. It aids in expansion of the space-charge region and strengthen the internal electric field across the MXene–g-C_3N_4 junction [87, 88]. This electric field promoted directional separation of photogenerated charge carriers by driving electrons toward the metallic MXene and concurrently forcing photogenerated holes toward the photoanode/electrolyte interface. As a result, accumulation of the interfacial holes increased facilitating direct oxidation of PMG molecules and surface-bound water species prior to bulk recombination. Such bias-assisted band bending and hole migration were well-established characteristics of Schottky-type PEC photoanodes and were critical in achieving high oxidation efficiencies under visible-light irradiation [89]. The degradation rate increased with applied potential up to 1.4 V, beyond which further increase resulted in a gradual decline in efficiency. At 1.4 V, nearly complete degradation was achieved within 270 min, whereas lower potentials (1.0 and 1.2 V) exhibited incomplete removal. The decline observed at higher potentials (1.6 and 1.8 V) can be attributed to the onset of competing anodic reactions, particularly the oxygen evolution reaction (OER) [90, 91]. At elevated potentials, the thermodynamically favorable OER increasingly consumes photogenerated holes at the anode surface, thereby suppressing interfacial charge transfer toward PMG oxidation. In addition, intensified OER can promote bubble formation and local mass-transfer limitations, further reducing the effective utilization of charge carriers for pollutant degradation [92]. Similar potential-dependent competition between OER and organic oxidation has been widely reported in PEC and electrocatalytic degradation systems. These observations indicated that an optimum bias potential of 1.4 V provides the best balance between charge separation efficiency and minimization of competing processes.

The effect of initial PMG concentration was also investigated in the range of 50 – 150 ppm (Figure 8d). A strong concentration dependence was observed where lower concentrations enabled more rapid and complete degradation. At 50 ppm, the pollutant was nearly eliminated within the reaction period. However, residual concentrations of ~12 and 20% retained in 100 and 150 ppm samples, respectively after 270 min. The reduced efficiency at higher concentrations is primarily due to increased competition for active sites on the catalyst surface. It is further influenced by stronger light scattering and absorption by PMG molecules, as well as possible mass transfer limitations. These findings confirmed that the developed catalyst system was highly effective at environmentally relevant pollutant levels.

Although optimization of catalyst loading and operating conditions would be necessary for higher concentration levels. COD analysis provides the amount of O_2 required to completely oxidize the organic matter present in the solution whereas TOC content provide how much of the organic carbon is left that can be converted to CO_2. After 270 mins of experiment COD and TOC removal analysis showed 85% and 70% removal, respectively. Lower TOC removal extent was observed compared to COD removal. It implies though majority of PMG is mineralized, some of it gets converted and exist into stable oxidized intermediates. Moreover, IC analysis was done over initial PMG samples and final degraded samples after 270 mins. IC graphs (Figure S8) have shown no presence of phosphate or nitrate ions in the initial PMG samples. In the final degraded samples phosphate and nitrate ions were observed with the concentration of nitrate ions much higher than phosphate ions. This confirms that most of the PMG is degrading via C-N cleavage producing AMPA and nitrate ions eventually. However, C-P bond is found to be much more resistant, resulting in less phosphate ions release. This finding is consistent with the COD and TOC analysis. These results suggest that while the current system is highly effective at higher concentrations, it could be potentially integrated with other effective techniques, such as biodegradation, to achieve complete and effective mineralization of PMG.

Scavenger experiments were performed to identify the dominant reactive species involved in PMG degradation. p-benzoquinone (BQ), isopropyl alcohol (IPA) and ethylenediaminetetraacetic acid disodium salt (EDTA-2Na) were used as selective quenchers for $^{\cdot}O_2^-$, $^{\cdot}OH$ and h^+, respectively (Figure S9). The addition of BQ reduced the degradation efficiency to 11.07%, indicating a strong inhibition of the PEC degradation process due to effective quenching of $^{\cdot}O_2^-$ radicals. In contrast, the presence of IPA resulted in 33.45% degradation, indicating lower contribution of $^{\cdot}OH$. However, the generation of $^{\cdot}OH$ from the CB of g-C_3N_4 is less likely due to the positioning of its VB. The oxidizing potential for H_2O to convert into $^{\cdot}OH$ is more positive than the E_{VB} of g-C_3N_4. The major pathway thus remains is conversion of $^{\cdot}O_2^-$ into $^{\cdot}OH$ via an oxidative pathway, resulting majorly in degradation of PMG.

In addition, a catalyst reusability study was performed to evaluate durability of the prepared photocatalyst. After each cycle of sequential batch experiments the PMG and electrolyte-laden water was replaced. The MXene-g-C_3N_4/ACF was thoroughly rinsed with DI water, before reusing the catalyst in the next run, to remove any mineralization products adsorbed on the catalyst surface. All the operating conditions, including

the time of degradation, were kept constant in each experiment. After 5 cycles of photocatalyst reuse the extent of degradation was almost unchanged. As shown in Figure S10, the degradation efficiency reached 93% in the final cycle post 22.5 h of cumulative operating time. It shows the remarkable reusability of the catalyst, indicating robust stability of heterojunction even under the strong acidic environment.

3.2. Proposed reaction mechanism

Under visible light irradiation, g-C_3N_4 absorbed photons and generated electron-hole pairs (Eq. 1). The photogenerated electrons migrated from the conduction band (CB) of g-C_3N_4 towards MXene surface owing to the Schottky barrier at the heterojunction interface. Such Schottky-type junction between MXene and g-C_3N_4 facilitated unidirectional electron transfer and suppress recombination, thereby enhancing photocatalytic efficiency [93].

$$g - C_3N_4 + h\nu \rightarrow e^-_{(CB)} + h^+_{(VB)} \quad \text{(Eq.1)}$$

Notably, MXene acted as an electron sink that effectively suppressed recombination and enabled continuous charge separation. This role of MXene as an efficient electron acceptor that traps photogenerated electrons and reduces recombination has also been reported previously [94]. A scheme of the proposed degradation pathway is presented in Figure 9. The accumulated electrons on the MXene surface reduce dissolved oxygen to $\cdot O_2^-$ (Eq. 2) that further participated in generating ·OH and other ROSs.

$$e^-_{(MXene)} + O_2 \rightarrow {}^{\bullet}O_2^- \quad \text{(Eq.2)}$$

The generated $\cdot O_2^-$ species underwent protonation to form hydroperoxyl radicals ($HO_2\cdot$s), followed by dismutation reactions producing H_2O_2 (Eq. 3a-b). The subsequent reduction of H_2O_2 led to the formation of highly reactive ·OH radicals (Eq. 3c). Similar oxygen-mediated ROS generation reactions have been reported in photocatalytic degradation of pollutants [95]. These ROSs, possessing strong oxidative potential, were primarily responsible for attacking the C–P, C–N, and C–C bonds of PMG.

$$^{\bullet}O_2^- + H^+ \rightarrow HO_2\bullet \quad \text{(Eq.3a)}$$

$$2HO_2^{\bullet} \rightarrow H_2O_2 + O_2 \quad \text{(Eq.3b)}$$

$$H_2O_2 + e^- \rightarrow {}^{\bullet}OH + OH^- \quad \text{(Eq.3c)}$$

The successive oxidation steps converted PMG to intermediate products such as AMPA and glyoxylic acid (Eq. 4). With prolonged irradiation, these intermediates undergo further breakdown, ultimately yielding CO_2, H_2O, and inorganic ions such as PO_4^{3-} and NO_3^- (Eq. 5).

$$C_3H_8NO_5P + H_2O \rightarrow CH_6NO_3P + C_2H_2O_3 + 2H^+ + 2e^- \quad \text{(Eq.4)}$$

$$C_3H_8NO_5P + 14{}^{\bullet}OH \rightarrow 3CO_2 + H_2O + H_2PO_4^- + NO_3^- + 6H^+ + 6e^- \quad \text{(Eq.5)}$$

The MXene–g-C_3N_4 Schottky junction efficiently directed electron transfer, stabilized charge carriers, and sustained ROSs generation, enabling complete PEC degradation of PMG through sequential oxidation and mineralization. This finding is also in coherence with the fact that decreasing of pH is resulting in increment of the PMG removal. It should also be noted that quenching of ·OH has less effect than quenching of $\cdot O_2^-$, indicating that superoxide radicals are also contributing in direct degradation of PMG. Using EDTA-2Na for quenching h^+ resulted in degradation efficiency of 90%. The slight decrement in the degradation efficiency can be attributed to the direct oxidation of PMG via h^+ at the VB of g-C_3N_4. Moreover, holes accumulated at the VB of g-C_3N_4 has liekly oxidize water molecules to O_2. These mechanistic insights not only clarify the pathway of pollutant breakdown but also underscore the central role of interfacial charge dynamics in driving efficient degradation.

4. Conclusions

A MXene–g-C_3N_4/ACF photoanode was successfully fabri-

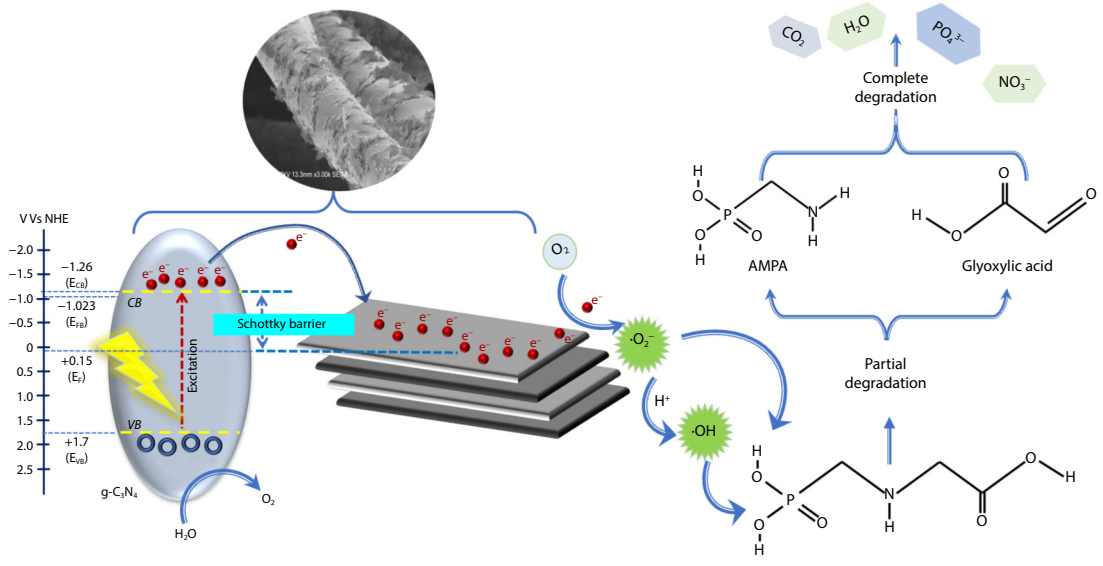

Fig. 9. Proposed PEC degradation mechanism of PMG over the MXene–g-C_3N_4 Schottky junction photoanode.

cated to develop a Schottky-type heterojunction for PEC degradation of PMG. Physico-chemical and electrochemical analyses showed strong interfacial coupling and formation of heterojunction between g-C_3N_4 and MXene. Mott-Schottky analysis confirmed that g-C_3N_4 behaves as an n-type semiconductor and indicated a band alignment that promotes electron transfer toward MXene. Furthermore, transient photocurrent measurement demonstrated an improved charge separation within the heterojunction. Under visible light along with applied bias, the system exhibited excellent photoelectrochemical synergistic effect, leading to nearly complete degradation of PMG within 270 min at an ideal potential of 1.4 V. Applying an external bias enhanced band bending at the metal-semiconductor interface. It improved the charge separation and promoted oxidation reactions at the interface. Control experiments showed that adsorption of PMG on ACF contributed minimally to removal of pollutant. Separate scavenger experiments revealed that superoxide radicals ($\bullet O_2^-$) were the dominant reactive species responsible for the degradation of PMG. Mineralization analysis showed COD and TOC removal of 85 and 70% respectively. This process also accompanied by the formation of nitrate and phosphate ions detected by ion chromatography. These findings suggested that the MXene–g-C_3N_4 Schottky heterojunction effectively promotes the charge separation and ROS generation. As a result, it offers an effective approach for the PEC degradation of persistent herbicides in aqueous systems. Although the system achieved significant degradation along with partial mineralization, further study is needed to improve mineralization efficiency. It is also important to evaluate its performance in real water matrices where competing ions and natural organic matter may affect the process. These investigations will be essential to validate the practical applicability of MXene–g-C_3N_4 PEC systems for treatment of herbicide-contaminated water.

Acknowledgement

Dr. Priyanka Gupta gratefully acknowledges the Department of Science and Technology, Government of India, for supporting her research through the INSPIRE Faculty Fellowship and Research Grant (IFA-22-ENG-345). She also thanks the Department of Chemical Engineering at Indian Institute of Technology as well as at Harcourt Butler Technical University, Kanpur, for hosting her and providing laboratory facilities. She is also grateful to Anusandhan National Research Foundation for awarding her research grant (project no.: ANRF/ECRG/2024/000412/ENS) to support her research.

Conflict of interest

The authors declare that there are no known financial, personal, or professional conflicts of interest that could have influenced the content, analysis, or conclusions presented in this manuscript.

Electronic Supplementary Material (ESM)

The online version contains supplementary material available at https://doi.org/10.26599/ECS.2026.9600024.

References

[1] Bou Mitri, C.; Dagher, S.; Makkawi, A.; Khreyss, Z.; Hassan, H. F. Glyphosate in food: A narrative review. *J. Agric. Food Res.*, 2025, 19: 101643.

[2] Bonansea, R. I., Filippi, I.; Wunderlin, D. A., Marino, D. J. G., Amé, M. V. The fate of glyphosate and AMPA in a freshwater endorheic basin: An ecotoxicological risk assessment. *Toxics*, 2018, 6: 3.

[3] Botta, F.; Lavison, G.; Couturier, G.; Alliot, F.; Moreau-Guigon, E.; Fauchon, N.; Guery, B.; Chevreuil, M.; Blanchoud, H. Transfer of glyphosate and its degradate AMPA to surface waters through urban sewerage systems. *Chemosphere*, 2009, 77: 133–139.

[4] E. Kujawski, A. Nowakowski, Glyphosate is polluting our waters-all across Europe, (2023).

[5] Manassero, A.; Passalia, C.; Negro, A. C.; Cassano, A. E.; Zalazar, C. S. Glyphosate degradation in water employing the H_2O_2/UVC process. *Water Res.*, 2010, 44: 3875–3882.

[6] Lu, J.; Zhang, C.; Wang, W. G.; Xu, W. P.; Chen, W. D.; Tao, L. M.; Li, Z.; Zhang, Y.; Cheng, J. G. Exposure to environmental concentrations of glyphosate induces cardiotoxicity through cellular senescence and reduced cell proliferation capacity. *Ecotoxicol. Environ. Saf.*, 2023, 261: 115112.

[7] Despotović, S. G., Gavrilović, B. R., Radovanović, T. B., Petrović, T. G., Ajduković, M.; Vučić, T.; Cvijanović, M.; Mašković, P. Z., Mašković, J. M., Prokić, M. D., et al. Effects of glyphosate-based herbicide on oxidative stress and neurotoxicity parameters in newt (Triturus ivanbureschi) larvae under temperature changes predicted by future climate scenarios. *Ecotoxicol. Environ. Saf.*, 2025, 303: 118969.

[8] Brodeur, J. C., Poletta, G. L., Simoniello, M. F., Carriquiriborde, P.; Cristos, D. S., Pautasso, N.; Paravani, E.; Poliserpi, M. B., D'Andrea, M. F., Gonzalez, P. V., et al. The problem with implementing fish farms in agricultural regions: A trial in a pampean pond highlights potential risks to both human and fish health. *Chemosphere*, 2021, 262: 128408.

[9] Brovini, E. M., Cardoso, S. J., Quadra, G. R., Vilas-Boas, J. A., Paranaíba, J. R., de Oliveira Pereira, R.; Mendonça, R. F. Glyphosate concentrations in global freshwaters: Are aquatic organisms at risk *Environ. Sci. Pollut. Res.*, 2021, 28: 60635–60648.

[10] Reichert, L. M. M., de Oliveira, D. R., Papaleo, J. L., Valgas, A. A. N., Oliveira, G. T. Biochemical and body condition markers in Rhinella icterica tadpoles exposed to atrazine, glyphosate, and quinclorac based herbicides in ecologically relevant concentrations. *Environ. Toxicol. Pharmacol.*, 2022, 93: 103884.

[11] Martinez, A.; Al-Ahmad, A. J. Effects of glyphosate and aminomethylphosphonic acid on an isogeneic model of the human blood-brain barrier. *Toxicol. Lett.*, 2019, 304: 39–49.

[12] Newman, M. M., Hoilett, N.; Lorenz, N.; Dick, R. P., Liles, M. R., Ramsier, C.; Kloepper, J. W. Glyphosate effects on soil rhizosphere-associated bacterial communities. *Sci. Total Environ.*, 2016, 543: 155–160.

[13] Gandhi, K.; Khan, S.; Patrikar, M.; Markad, A.; Kumar, N.; Choudhari, A.; Sagar, P.; Indurkar, S. Exposure risk and environmental impacts of glyphosate: Highlights on the toxicity of herbicide co-formulants. *Environ. Chall.*, 2021, 4: 100149.

[14] Costas-Ferreira, C.; Durán, R.; Faro, L. R. F. Toxic effects of glyphosate on the nervous system: A systematic review. *Int. J. Mol. Sci.*, 2022, 23: 4605.

[15] Galli, F. S.; Mollari, M.; Tassinari, V.; Alimonti, C.; Ubaldi, A.; Cuva, C.; Marcoccia, D. Overview of human health effects related to glyphosate exposure. *Front. Toxicol.*, 2024, 6: 1474792.

[16] Gupta, P.; Verma, N. Evaluation of degradation and mineralization of glyphosate pollutant in wastewater using catalytic wet air oxidation over Fe-dispersed carbon nanofibrous beads. *Chem. Eng. J.*, 2021, 417: 128029.

[17] Thongprakaisang, S.; Thiantanawat, A.; Rangkadilok, N.; Suriyo, T.; Satayavivad, J. Glyphosate induces human breast cancer cells growth *via* estrogen receptors. *Food Chem. Toxicol.*, 2013, 59:

129–136.
[18] Feng, D.; Soric, A.; Boutin, O. Treatment technologies and degradation pathways of glyphosate: A critical review. *Sci. Total Environ.*, 2020, 742: 140559.
[19] Gupta, P.; Pandey, K.; Verma, N. Augmented complete mineralization of glyphosate in wastewater *via* microbial degradation post CWAO over supported Fe-CNF. *Chem. Eng. J.*, 2022, 428: 132008.
[20] Srivastava, A.; Jain, P.; Gupta, P. Understanding metabolic pathways for enhanced microbial electrosynthesis: A sustainable approach for carbon dioxide reduction to high–value products. *Chem. Eng. J. Adv.*, 2025, 22: 100755.
[21] Hu, Y. S.; Zhao, Y. Q.; Sorohan, B. Removal of glyphosate from aqueous environment by adsorption using water industrial residual. *Desalination*, 2011, 271: 150–156.
[22] Pereira, H. A., Hernandes, P. R. T., Netto, M. S., Reske, G. D., Vieceli, V.; Oliveira, L. F. S., Dotto, G. L. Adsorbents forglyphosate removalin contaminated waters: A review. *Environ. Chem. Lett.*, 2021, 19: 1525–1543.
[23] Xiao, G. Q.; Meng, Q. D. D151 resin preloaded with Fe^{3+} as a salt resistant adsorbent for glyphosate from water in the presence 16% NaCl. *Ecotoxicol. Environ. Saf.*, 2020, 190: 110140.
[24] Cardoso, I. M. F.; Cardoso, R. M. F.; da Silva, J. C. G. E. Advanced oxidation processes coupled with nanomaterials for water treatment. *Nanomaterials*, 2021, 11: 2045.
[25] Wu, H.; Sun, Q.; Chen, J. Y.; Wang, G. Y.; Wang, D.; Zeng, X. F.; Wang, J. X. Citric acid-assisted ultrasmall CeO_2 nanoparticles for efficient photocatalytic degradation of glyphosate. *Chem. Eng. J.*, 2021, 425: 130640.
[26] Tang, Q. Y.; Yang, M. J.; Yang, S. Y.; Xu, Y. H. Enhanced photocatalytic degradation of glyphosate over 2D CoS/BiOBr heterojunctions under visible light irradiation. *J. Hazard. Mater.*, 2021, 407: 124798.
[27] Zhang, W.; You, Q. Z.; Shu, J. K.; Wang, A. H.; Lin, H.; Yan, X. C. Photocatalytic degradation of glyphosate using Ce/N Co-doped TiO_2 with oyster shell powder as carrier under the simulated fluorescent lamp. *Front. Environ. Sci.*, 2023, 11: 1131284.
[28] Garcia-Muñoz, P.; Dachtler, W.; Altmayer, B.; Schulz, R.; Robert, D.; Seitz, F.; Rosenfeldt, R.; Keller, N. Reaction pathways, kinetics and toxicity assessment during the photocatalytic degradation of glyphosate and myclobutanil pesticides: Influence of the aqueous matrix. *Chem. Eng. J.*, 2020, 384: 123315.
[29] Yang, Y.; Deng, Q. Z.; Zhang, Y. L. Comparative study of low-index{1 0 1}-TiO_2, {0 0 1}-TiO_2, {1 0 0}-TiO_2 and high-index{2 0 1}-TiO_2 on glyphosate adsorption and photo-degradation. *Chem. Eng. J.*, 2019, 360: 1247–1254.
[30] Kumar, A.; Shrivastava, S.; Verma, N.; Hsueh, C. C.; Chang, C. T.; Chen, B. Y. Electrolyte-free electro-oxidation of aqueous glyphosate: CuPc-ACF electrode and optimization of operating parameters. *Process. Saf. Environ. Prot.*, 2020, 142: 260–271.
[31] He, R. A.; Liu, H. J.; Liu, H. M.; Xu, D. F.; Zhang, L. Y. S-scheme photocatalyst Bi_2O_3/TiO_2 nanofiber with improved photocatalytic performance. *J. Mater. Sci. Technol.*, 2020, 52: 145–151.
[32] Gupta, P.; Noori, M. T., Núñez, A. E., Verma, N. An insight into the bioelectrochemical photoreduction of CO_2 to value-added chemicals. *iScience*, 2021, 24: 102294.
[33] Emeline, A. V.; Rudakova, A. V.; Mikhaylov, R. V.; Bulanin, K. M.; Bahnemann, D. W. Photoactive heterostructures: How they are made and explored. *Catalysts*, 2021, 11: 294.
[34] Wang, X. T.; Ren, Y. Y.; Li, Y.; Zhang, G. K. Fabrication of 1D/2D $BiPO_4$/g-C_3N_4 heterostructured photocatalyst with enhanced photocatalytic efficiency for NO removal. *Chemosphere*, 2022, 287: 132098.
[35] Manna, S.; Remya, N.; Singhal, N. Advancements in S-scheme photocatalytic material for wastewater treatment. *J. Environ. Chem. Eng.*, 2023, 11: 109838.
[36] Bilal, M.; Alfaifi, M. Q.; Ben Ahmed, S.; Abduljawad, M. M.; Alrashed, Y. I.; Aldurahim, E. S.; Alassmy, Y. A. A review of strategies to switch heterojunction system from type-II to S-scheme for photocatalytic applications. *Mater. Sci. Semicond. Process.*, 2025, 186: 109051.
[37] Shabbir, A.; Sardar, S.; Mumtaz, A. Mechanistic investigations of emerging type-II, Z-scheme and S-scheme heterojunctions for photocatalytic applications–A review. *J. Alloys Compd.*, 2024, 1003: 175683.
[38] Zhang, X. Y.; Chen, Y. H.; Jin, Z. Q.; Jiang, H. S.; Li, Z.; Liu, Y.; Gao, Z.; Wang, X. Q. Direct Z-scheme In_2O_3/g-C_3N_4 nanocomposites: Breaking through the performance limitations of conventional type II heterojunctions for photocathodic protection of Q235 CS in 3. *5 wt% NaCl solution. J. Alloys Compd.*, 2024, 970: 172558.
[39] Zhang, L. Y.; Zhang, J. J.; Yu, H. G.; Yu, J. G. Emerging S-scheme photocatalyst. *Adv. Mater.*, 2022, 34: 2107668.
[40] Kumari, P.; Bahadur, N.; Kong, L. X.; O'Dell, L. A., Merenda, A.; Dumée, L. F. Engineering Schottky-like and heterojunction materials for enhanced photocatalysis performance–a review. *Mater. Adv.*, 2022, 3: 2309–2323.
[41] Xiao, J. D.; Han, L. L.; Luo, J.; Yu, S. H.; Jiang, H. L. Integration of plasmonic effects and Schottky junctions into metal–organic framework composites: Steering charge flow for enhanced visible-light photocatalysis. *Angew. Chem. Int. Ed.*, 2018, 57: 1103–1107.
[42] Cao, Y. M.; Yue, L.; Li, Z. X.; Han, Y. H.; Lian, J.; Qin, H. P.; He, S. Y. Construction of Sn-Bi-MOF/Ti3C2 Schottky junction for photocatalysis of tetracycline: Performance and degradation mechanism. *Appl. Surf. Sci.*, 2023, 609: 155191.
[43] Liu, Q. X.; Ai, L. H.; Jiang, J. MXene-derived TiO_2@C/g-C_3N_4 heterojunctions for highly efficient nitrogen photofixation. *J. Mater. Chem. A*, 2018, 6: 4102–4110.
[44] Hou, H. L.; Shao, G.; Yang, W. Y. Recent advances in g-C_3N_4-based photocatalysts incorporated by MXenes and their derivatives. *J. Mater. Chem. A*, 2021, 9: 13722–13745.
[45] He, F.; Mao, Y. Y.; Hu, Y.; Wu, J. Y.; Xie, E. Q.; Wang, Z. X.; Li, Y. X. The synthesis of 3D organic–inorganic hybrid heterojunctions of g-C_3N_4 nanoneedles@Ti_3C_2 MXene with superior photocatalytic H_2 evolution. *Chem. Commun.*, 2024, 60: 11347–11350.
[46] Biswal, L.; Nayak, S.; Parida, K. Recent progress on strategies for the preparation of 2D/2D MXene/g-C_3N_4 nanocomposites for photocatalytic energy and environmental applications. *Catal. Sci. Technol.*, 2021, 11: 1222–1248.
[47] Yang, Y.; Zeng, Z. T.; Zeng, G. M.; Huang, D. L.; Xiao, R.; Zhang, C.; Zhou, C. Y.; Xiong, W. P.; Wang, W. J.; Cheng, M. et al. Ti3C2 Mxene/porous g-C_3N_4 interfacial Schottky junction for boosting spatial charge separation in photocatalytic H_2O_2 production. *Appl. Catal. B Environ.*, 2019, 258: 117956.
[48] Bai, L. Q.; Huang, H. W.; Yu, S. X.; Zhang, D. Y.; Huang, H. T.; Zhang, Y. H. Role of transition metal oxides in g-C_3N_4-based heterojunctions for photocatalysis and supercapacitors. *J. Energy Chem.*, 2022, 64: 214–235.
[49] Huang, D. L.; Li, Z. H.; Zeng, G. M.; Zhou, C. Y.; Xue, W. J.; Gong, X. M.; Yan, X. L.; Chen, S.; Wang, W. J.; Cheng, M. Megamerger in photocatalytic field: 2D g-C_3N_4 nanosheets serve as support of 0D nanomaterials for improving photocatalytic performance. *Appl. Catal. B Environ.*, 2019, 240: 153–173.
[50] Xu, Y. J.; Wang, S.; Yang, J.; Han, B.; Nie, R.; Wang, J. X.; Dong, Y. P.; Yu, X. G.; Wang, J. G.; Jing, H. W. Highly efficient photoelectrocatalytic reduction of CO_2 on the Ti_3C_2/g-C_3N_4heterojunction with rich Ti^{3+} and pyri-N species. *J. Mater. Chem. A*, 2018, 6: 15213–15220.
[51] Gupta, P.; Singh, M.; Noori, M. T., Jack, J. Microbial photo electrosynthesis for efficient CO_2 conversion using MXenes: Materials, mechanisms, and applications. *J. Environ. Chem. Eng.*, 2024, 12:

113063.
[52] Gupta, P.; Verma, N. Conversion of CO_2 to formate using activated carbon fiber-supported g-C_3N_4-$NiCoWO_4$ photoanode in a microbial electrosynthesis system. *Chem. Eng. J.*, 2022, 446: 137029.
[53] Shen, X. F.; Zhang, T. Y.; Xu, P. F.; Zhang, L. S.; Liu, J. S.; Chen, Z. G. Growth of C_3N_4 nanosheets on carbon-fiber cloth as flexible and macroscale filter-membrane-shaped photocatalyst for degrading the flowing wastewater. *Appl. Catal. B Environ.*, 2017, 219: 425–431.
[54] Limbu, T. B.; Chitara, B.; Orlando, J. D.; Garcia Cervantes, M. Y.; Kumari, S.; Li, Q.; Tang, Y. A.; Yan, F. Green synthesis of reduced $Ti_3C_2T_x$ MXene nanosheets with enhanced conductivity, oxidation stability, and SERS activity. *J. Mater. Chem. C*, 2020, 8: 4722–4731.
[55] Zaed, M. A.; Cherusseri, J.; Saidur, R.; Tan, K. H.; Pandey, A. K. Synthesis and characterization of hierarchical $Ti_3C_2T_x$ MXene/graphitic-carbon nitride/activated carbon@luffa sponge composite for enhanced water desalination. *Open Ceram.*, 2024, 19: 100645.
[56] Alulema-Pullupaxi, P.; Fernández, L.; Debut, A.; Santacruz, C. P.; Villacis, W.; Fierro, C.; Espinoza-Montero, P. J. Photoelectrocatalytic degradation of glyphosate on titanium dioxide synthesized by sol-gel/spin-coating on boron doped diamond (TiO_2/BDD) as a photoanode. *Chemosphere*, 2021, 278: 130488.
[57] Samsudin, M. F. R., Ullah, H.; Bashiri, R.; Mohamed, N. M., Sufian, S.; Ng, Y. H. Experimental and DFT insights on microflower g-C_3N_4/BiVO4 photocatalyst for enhanced photoelectrochemical hydrogen generation from lake water. *ACS Sustainable Chem. Eng.*, 2020, 8(25): 9393–9403.
[58] Nasri, M. S. I.; Samsudin, M. F. R.; Ali Tahir, A.; Sufian, S. Effect of MXene loaded on g-C_3N_4 photocatalyst for the photocatalytic degradation of methylene blue. *Energies*, 2022, 15: 955.
[59] Valipour, A.; Hamnabard, N.; Meshkati, S. M. H., Pakan, M.; Ahn, Y. H. Effectiveness of phase- and morphology-controlled MnO_2 nanomaterials derived from flower-like δ-MnO_2 as alternative cathode catalyst in microbial fuel cells. *Dalton Trans.*, 2019, 48: 5429–5443.
[60] Shtarev, D. S., Shtareva, A. V., Ryabchuk, V. K., Rudakova, A. V., Serpone, N. Considerations of trends in heterogeneous photocatalysis. correlations between conduction and valence band energies with bandgap energies of various photocatalysts. *ChemCatChem*, 2019, 11: 3534–3541.
[61] LaChance, R.; Adeli, B.; Taghipour, F. Solar fuel generation by 2D self-assembled g-C_3N_4/BiVO4 Z-scheme. *Sol. RRL*, 2024, 8: 2300677.
[62] Ran, J. R.; Gao, G. P.; Li, F. T.; Ma, T. Y.; Du, A. J.; Qiao, S. Z. Ti3C2 MXene co-catalyst on metal sulfide photo-absorbers for enhanced visible-light photocatalytic hydrogen production. *Nat. Commun.*, 2017, 8: 13907.
[63] Liu, Y.; Zheng, Z. S.; Li, Y. L.; Xi, K. B.; Mi, Y. S. PI/g-C_3N_4 composite photocatalyst with enhanced activity of degrading pollutants under visible light. *J. Mater. Sci.*, 2021, 56: 9122–9133.
[64] Wong, K. T.; Kim, S. C.; Yun, K.; Choong, C. E.; Nah, I. W.; Jeon, B. H.; Yoon, Y.; Jang, M. Understanding the potential band position and E–/ h+ separation lifetime for Z-scheme and type-II heterojunction mechanisms for effective micropollutant mineralization: Comparative experimental and DFT studies. *Appl. Catal. B Environ.*, 2020, 273: 119034.
[65] Martín-Ramos, P.; Martín-Gil, J.; Dante, R. C., Vaquero, F.; Navarro, R. M., Fierro, J. L. G. A simple approach to synthesize g-C_3N_4 with high visible light photoactivity for hydrogen production. *Int. J. Hydrog. Energy*, 2015, 40: 7273–7281.
[66] Chin, J. Y.; Ahmad, A. L.; Low, S. C. Graphitic carbon nitride photocatalyst for the degradation of oxytetracycline hydrochloride in water. *Mater. Chem. Phys.*, 2023, 301: 127626.
[67] Ragupathi, V.; Panigrahi, P.; Ganapathi Subramaniam, N. Bandgap engineering in graphitic carbon nitride: Effect of precursors. *Optik*, 2020, 202: 163601.
[68] Nihal, Kumari, C.; Sharma, R.; Sharma, M.; Dogra, S. D.; Sharma, I.; Choudhary, B. C.; Goswamy, J. K. gCN/ZnO nanocomposite as an efficient sunlight active photocatalyst for Rhodamine B dye degradation. *Hybrid Adv.*, 2025, 8: 100346.
[69] Florentino-Madiedo, L.; Díaz-Faes, E.; Barriocanal, C. Relationship between gCN structure and photocatalytic water splitting efficiency. *Carbon*, 2022, 187: 462–476.
[70] Saha, U.; Jaiswal, R.; Goswami, T. H.; Maji, P. K. Cobalt ferrite ($CoFe_2O_4$)–activated carbon fabric (ACF) based composite electrode material for supercapacitor application. *J. Energy Storage*, 2024, 99: 113218.
[71] Sharma, S.; Gupta, M. K.; Singh, V. K. Observation of band gap enhancement and green–yellow emission of thermally stable MXene nanosheets. *Opt. Mater.*, 2024, 155: 115780.
[72] Attri, P.; Garg, P.; Sharma, P.; Singh, R.; Chauhan, M.; Lim, D. K.; Kumar, S.; Chaudhary, G. R. Precursor-dependent fabrication of exfoliated graphitic carbon nitride (gCN) for enhanced photocatalytic and antimicrobial activity under visible light irradiation. *J. Clean. Prod.*, 2023, 422: 138538.
[73] Niu, P.; Zhang, L. L.; Liu, G.; Cheng, H. M. Graphene-like carbon nitride nanosheets for improved photocatalytic activities. *Adv. Funct. Mater.*, 2012, 22: 4763–4770.
[74] Haq, Y. U.; Ullah, R.; Mazhar, S.; Khattak, R.; Ali Qarni, A.; Haq, Z. U.; Amin, S. Synthesis and characterization of 2D MXene: Device fabrication for humidity sensing. *J. Sci. Adv. Mater. Devices*, 2022, 7: 100390.
[75] Wen, Y. Y.; Rufford, T. E.; Chen, X. Z.; Li, N.; Lyu, M. Q.; Dai, L. M.; Wang, L. Z. Nitrogen-doped $Ti_3C_2T_x$ MXene electrodes for high-performance supercapacitors. *Nano Energy*, 2017, 38: 368–376.
[76] Patterson, A. L. The scherrer formula for X-ray particle size determination. *Phys. Rev.*, 1939, 56: 978–982.
[77] Shi, Z. Y.; Rao, L.; Wang, P. F.; Zhang, L. X. Influences of different carbon substrates on the morphologies of carbon/g-C_3N_4 photocatalytic composites and the purification capacities of different composites in the weak UV underwater environment. *Chemosphere*, 2022, 308: 136257.
[78] Cao, S. W.; Huang, Q.; Zhu, B. C.; Yu, J. G. Trace-level phosphorus and sodium co-doping of g-C 3 N_4 for enhanced photocatalytic H_2 production. *J. Power Sources*, 2017, 351: 151–159.
[79] Natu, V.; Benchakar, M.; Canaff, C.; Habrioux, A.; Célérier, S.; Barsoum, M. W. A critical analysis of the X-ray photoelectron spectra of Ti3C2Tz MXenes. *Matter*, 2021, 4: 1224–1251.
[80] Schultz, T.; Frey, N. C., Hantanasirisakul, K.; Park, S.; May, S. J., Shenoy, V. B., Gogotsi, Y.; Koch, N. Surface termination dependent work function and electronic properties of $Ti_3C_2T_x$ MXene. *Chem. Mater.*, 2019, 31(17): 6590–6597.
[81] Persson, I.; Näslund, L. Å.; Halim, J.; Barsoum, M. W., Darakchieva, V.; Palisaitis, J.; Rosen, J.; Persson, P. O. Å. On the organization and thermal behavior of functional groups on Ti3C2 MXene surfaces in vacuum. *2D Mater.*, 2018, 5(1): 015002.
[82] Ashok, A.; Saseendran, S. B., Asha, A. S. Synthesis of $Ti_3C_2T_x$ MXene from the Ti_3AlC_2 MAX phase with enhanced optical and morphological properties by using ammonia solution with the *in-situ* HF forming method. *Phys. Scr.*, 2022, 97(2): 025807.
[83] Yang, S. Y.; Li, L.; Xiao, T.; Zheng, D.; Zhang, Y. T. Role of surface chemistry in modified ACF (activated carbon fiber)-catalyzed peroxymonosulfate oxidation. *Appl. Surf. Sci.*, 2016, 383: 142–150.
[84] Wei, J. L.; Fang, T.; Shiraiwa, M. Effects of acidity on reactive oxygen species formation from secondary organic aerosols. *ACS Environ. Au*, 2022, 2(4): 336–345.
[85] Park, H.; Kim, H. I.; Moon, G. H.; Choi, W. Photoinduced charge transfer processes in solar photocatalysis based on modified

TiO_2. *Energy Environ. Sci.*, 2016, 9: 411–433.

[86] Thangavel, N.; Pandi, K.; Mahammed Shaheer, A. R.; Neppolian, B. Surface-state-induced upward band bending in P doped g-C_3N_4 for the formation of an isotype heterojunction between bulk g-C_3N_4 and P doped g-C_3N_4: Photocatalytic hydrogen production. *Catal. Sci. Technol.*, 2020, 10: 8015–8025.

[87] Yang, W. G.; Shen, D. Y.; Duan, Y. T.; Li, H. Y.; Li, J. M.; Li, Y. Enhanced photoelectrochemical water splitting through synergistic carrier separation and transfer in TiO_2-ferrihydrite-MXene nanowire arrays. *ACS Appl. Energy Mater.*, 2024, 7(10): 4412–4420.

[88] Ma, X. M.; Ma, Z.; Zhang, H. G.; Lu, D. Z.; Duan, J. Z.; Hou, B. R. Interfacial Schottky junction of $Ti_3C_2T_x$ MXene/g-C_3N_4 for promoting spatial charge separation in photoelectrochemical cathodic protection of steel. *J. Photochem. Photobiol. A Chem.*, 2022, 426: 113772.

[89] Jeon, T. H., Kim, H.; Kim, H. I.; Choi, W. Highly durable photoelectrochemical H_2O_2 production *via* dual photoanode and cathode processes under solar simulating and external bias-free conditions. *Energy Environ. Sci.*, 2020, 13: 1730–1742.

[90] Arts, A.; de Groot, M. T.; van der Schaaf, J. Current efficiency and mass transfer effects in electrochemical oxidation of C1 and C2 carboxylic acids on boron doped diamond electrodes. *Chem. Eng. J. Adv.*, 2021, 6: 100093.

[91] Umukoro, E. H., Peleyeju, M. G., Idris, A. O., Ngila, J. C., Mabuba, N.; Rhyman, L.; Ramasami, P.; Arotiba, O. A. Photoelectrocatalytic application of palladium decorated zinc oxide-expanded graphite electrode for the removal of 4-nitrophenol: Experimental and computational studies. *RSC Adv.*, 2018, 8: 10255–10266.

[92] Garcia-Segura, S.; Brillas, E. Applied photoelectrocatalysis on the degradation of organic pollutants in wastewaters. *J. Photochem. Photobiol. C Photochem. Rev.*, 2017, 31: 1–35.

[93] Otgonbayar, Z.; Oh, W. C. Synthesis of 2D/2D structural Ti3C2 MXene/g-C_3N_4 *via* the Schottky junction with metal oxides: Photocatalytic CO_2 reduction with a cationic scavenger. *Appl. Mater. Today*, 2023, 32: 101814.

[94] Zhou, Y. F.; Yu, M. C.; Zhan, R. N.; Wang, X. J.; Peng, G. W.; Niu, J. F. Ti3C2 MXene-induced interface electron separation in g-C_3N_4/Ti3C2 MXene/$MoSe_2$ Z-scheme heterojunction for enhancing visible light-irradiated enoxacin degradation. *Sep. Purif. Technol.*, 2021, 275: 119194.

[95] de J Silerio-Vázquez, F.; García-Roig, M.; González-Burciaga, L. A.; Núñez-Núñez, C. M.; Proal-Nájera, J. B. Glyphosate photocatalytic degradation: Exploring trends, innovations and research gaps. *J. Water Process. Eng.*, 2024, 66: 105948.